

Quantum dynamics of the Néel vector in the antiferromagnetic molecular wheel CsFe₈

O. Waldmann,^{1,*} C. Dobe,¹ H. U. Güdel,¹ and H. Mutka²

¹*Department of Chemistry and Biochemistry, University of Bern, CH-3012 Bern, Switzerland*

²*Institut Laue-Langevin, 6 rue Jules Horowitz, BP 156, 38042 Grenoble Cedex 9, France*

(Dated: August 28, 2018)

The inelastic neutron scattering (INS) spectrum is studied for the antiferromagnetic molecular wheel CsFe₈, in the temperature range 2 - 60 K, and for transfer energies up 3.6 meV. A qualitative analysis shows that the observed peaks correspond to the transitions between the L -band states, from the ground state up to the $S = 5$ multiplet. For a quantitative analysis, the wheel is described by a microscopic spin Hamiltonian (SH), which includes the nearest-neighbor Heisenberg exchange interactions and uniaxial easy-axis single-ion anisotropy, characterized by the constants J and D , respectively. For a best-fit determination of J and D , the L band is modeled by an effective SH, and the effective SH concept extended such as to facilitate an accurate calculation of INS scattering intensities, overcoming difficulties with the dimension of the Hilbert space. The low-energy magnetism in CsFe₈ is excellently described by the generic SH used. The two lowest states are characterized by a tunneling of the Néel vector, as found previously, while the higher-lying states are well described as rotational modes of the Néel vector.

PACS numbers: 75.10.Jm, 71.70.-d

I. INTRODUCTION

Molecular nanomagnets have recently attracted enormous attention, as these perfect magnetic nanoclusters were demonstrated to exhibit a number of spectacular quantum phenomena. In systems such as the single-molecule magnets Mn₁₂ and Fe₈, quantum tunneling of the magnetization, and related effects such as quantum interference, were observed.^{1,2,3,4,5} These phenomena are intimately connected to a high-spin ground state, so that at low temperatures these clusters essentially behave like large single spins S , where $S = 10$ for Mn₁₂ and Fe₈. This single-spin (or giant-spin) model is in fact extremely successful in describing the magnetism of single-molecule magnets.⁵ The actual underlying many-spin nature of the system, despite providing a large S , is not key to the observed tunneling phenomena.

Another class of interesting molecules are the antiferromagnetic (AFM) wheels, in which the magnetic centers are arranged into almost perfect rings (only wheels with an even number of equivalent spin centers shall be considered).^{6,7,8,9} A variety of quantum phenomena were observed, such as magnetization steps,^{6,10,11,12,13,14} quantized rotation of the Néel vector or quantized spin waves,¹⁵ and quantum tunneling of the Néel vector.^{16,17} In AFM wheels, in contrary to single-molecule magnets, the ground state has a total spin of $S = 0$ and hence is nonmagnetic. A single-spin model (with $S = 0$) would thus be inappropriate as it would not allow one to describe the interesting spin dynamics in these systems, which are manifestly many-spin effects. The lowest-lying excitations can be described in terms of the Néel vector, \mathbf{n} , which is essentially a vector parallel to the magnetization of one of the AFM sublattices [in a classical picture it could be for example parallel to the up-pointing spins as in Fig. 1(b)].

The magnetism of the AFM wheels is very well de-

scribed by the generic spin Hamiltonian

$$\hat{H} = -J \left(\sum_{i=1}^{N-1} \hat{\mathbf{S}}_i \cdot \hat{\mathbf{S}}_{i+1} + \hat{\mathbf{S}}_N \cdot \hat{\mathbf{S}}_1 \right) + D \sum_{i=1}^N \hat{S}_{i,z}^2, \quad (1)$$

which includes isotropic (Heisenberg) nearest-neighbor exchange interactions, characterized by the coupling constant $J < 0$, and an uniaxial magnetic anisotropy, of the easy-axis type, described by an on-site anisotropy with $D < 0$.¹⁸ N is the number of spin centers, $\hat{\mathbf{S}}_i$ is the spin operator of the i th ion with spin s , and z is the uniaxial anisotropy axis perpendicular to the plane of the wheel.

At small magnetic anisotropy, the lowest-lying excitations are characterized by a (quantized) rotation of the Néel vector, which in the quantum mechanical energy spectrum shows up as a low-lying rotational mode, the L band. This band is comprised of the lowest state in each S sector, i.e., the lowest $S = 0, 1, 2, \dots$ states, and their energies increase quadratically with S according to $E(S) \propto S(S+1)$.^{9,19,20,21,22} At higher energies, further rotational modes exist, collectively denoted as E

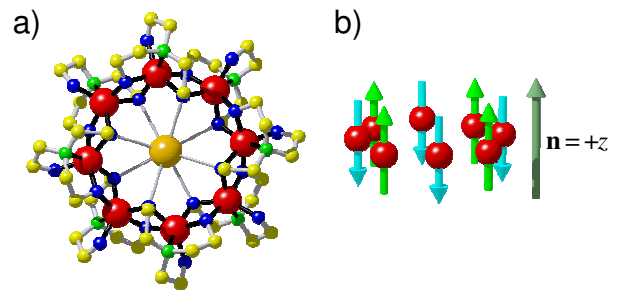


FIG. 1: (Color online) (a) Crystal structure of CsFe₈ [with Fe as dark gray spheres (red online) and H atoms omitted]. (b) Classical ground-state spin configuration for the Néel vector [long up arrow (dark green online)] oriented in the $+z$ direction.

band, which correspond to the quantized spin-wave excitations expected in AFM spin systems.^{9,19,22} This picture of the excitations has been demonstrated in great detail experimentally by inelastic neutron scattering (INS) on the AFM wheel Cr_8 (for which $J = -1.46$ meV, $D = -0.038$ meV, or $S_0/\hbar \equiv N_s\sqrt{2D/J} = 2.7$).^{15,23}

If the magnetic anisotropy becomes strong, and exceeds the threshold $S_0/\hbar > 4$,²³ the situation changes completely for the lowest lying excitation, which is then characterized by quantum tunneling of the Néel vector.^{24,25,26} This scenario has recently been observed by INS in the title compound, the AFM wheel CsFe_8 [the structure is shown in Fig. 1(a), here $J = -1.80$ meV, $D = -0.05$ meV, or $S_0/\hbar = 4.7$].¹⁶

In this work, the AFM wheel CsFe_8 is further investigated by INS measurements, extending the previous work, Ref. 16, to a larger temperature and energy transfer range, which allows us to probe a much larger part of the low-lying energy spectrum. In particular, the L -band states have been detected from the ground state up to the $S = 5$ multiplet at an energy of ca. 15 meV. This provides a detailed insight into the dynamics of the Néel vector in the CsFe_8 wheel.

In the next section II, the experimental details and the data are presented. The analysis of the data has been split into two parts. Initially, a qualitative analysis is provided in section III. Subsequently, in section IV some preparatory work for a quantitative analysis is developed, with the final analysis presented in section V. Section VI provides a discussion of the results, and the manuscript concludes in section VII.

II. EXPERIMENTAL

The CsFe_8 material, which has the chemical formula $[\text{CsFe}_8\text{L}_8]\text{Cl} \cdot 2\text{CHCl}_3 \cdot 0.5\text{CH}_2\text{Cl}_2 \cdot 0.75\text{L} \cdot 2.5\text{H}_2\text{O}$, with $\text{L} = \text{N}(\text{CH}_2\text{CH}_2\text{O})_3$, was prepared by the same procedure as in Ref. 27, but crystallized from a 1:1 mixture of CHCl_3 and CH_2Cl_2 by pentane vapor diffusion. The compound crystallizes in the monoclinic space group $\text{Pna}2_1$, and the molecules exhibit approximate C_4 symmetry with Fe-Fe distances of 3.142 - 3.164 Å, Fig. 1(a). The INS spectrum of CsFe_8 was measured with the time-of-flight spectrometer IN5 at the Institute Laue-Langevin (ILL), Grenoble, France. 4 g of a non-deuterated powder sample was sealed under a helium atmosphere in a double-walled hollow Al cylinder (50 mm in height, 16 mm external diameter, and 2 mm thickness) and inserted in a standard ILL orange ^4He cryostat. INS spectra were recorded at temperatures between 2.2 K and 60 K for incident neutron wavelengths of $\lambda = 3.8$ Å and 5.0 Å (energy resolution at the elastic peak was 161 μeV and 121 μeV , respectively). The data were corrected for detector efficiency using a vanadium standard; no further corrections were applied. The data shown correspond to the sum over all detector banks; the error bars are smaller than the symbol size.

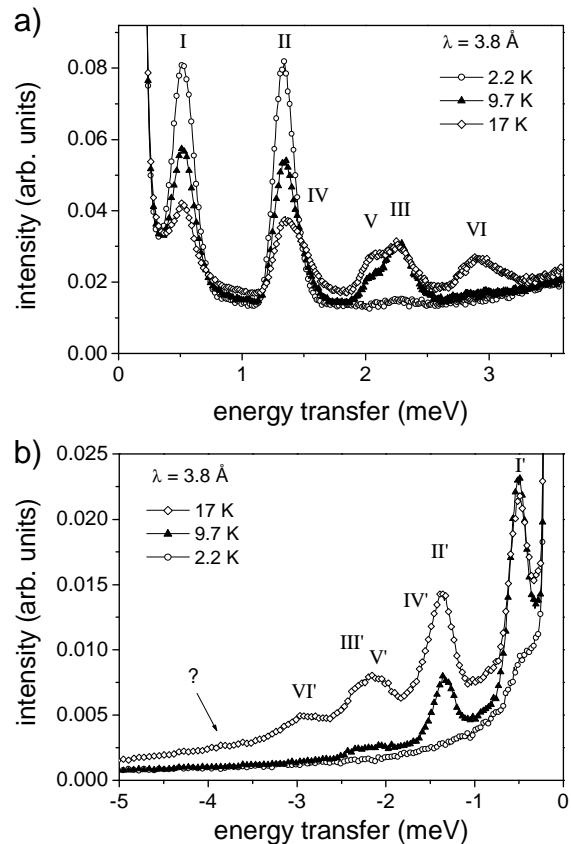


FIG. 2: Inelastic neutron scattering spectra of CsFe_8 at $T = 2.2$ K, 9.7 K, and 17 K, measured with $\lambda = 3.8$ Å. Panel (a) shows the neutron energy-loss, and panel (b) the neutron energy-gain side of the spectrum. The question mark indicates a weak feature which will be identified as a further transition VII' later on.

Figure 2 presents the neutron energy-loss and energy-gain sides of the INS spectrum as measured at $\lambda = 3.8$ Å for the temperatures $T = 2.2$ K, 9.7 K, and 17 K. Figure 3 presents the $\lambda = 5.0$ Å data obtained for the temperatures $T = 2.4$ K, 9.7 K, 17 K, and 60 K.

III. QUALITATIVE ANALYSIS

The interpretation of the INS spectra is relatively straightforward. In the 3.8 Å neutron energy-loss spectrum at 2.2 K, Fig. 2(a), two peaks I and II at about 0.5 meV and 1.3 meV, respectively, are observed. They correspond to transitions from the ground state to two next higher-lying levels at the corresponding excitation energies, as indicated in Fig. 4(a). At 9.7 K the intensities of peaks I and II decrease, and a new transition III at 2.3 meV develops, which is assigned to a transition from the first excited level to a higher-lying level at 2.8 meV. Some additional weaker features at 1.5 meV and 2.0 meV (peaks IV and V) are visible, which grow stronger at 17 K. They are assigned to transitions from

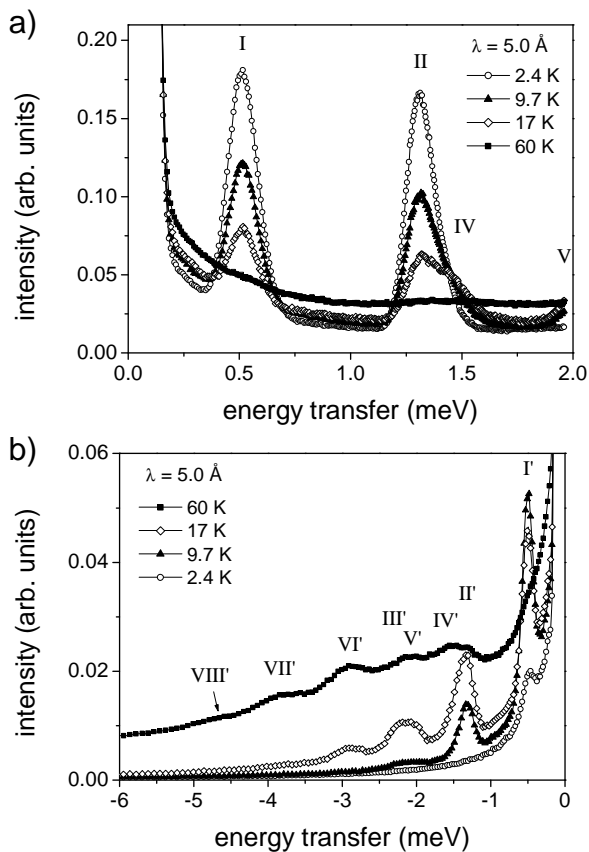


FIG. 3: Inelastic neutron scattering spectra of CsFe_8 at $T = 2.4$ K, 9.7 K, 17 K, and 60 K, measured with $\lambda = 5.0$ Å. Panel (a) shows the neutron energy-loss, and panel (b) the neutron energy-gain side of the spectrum.

the second excited level to higher-lying levels at again 2.8 meV and 3.3 meV. At 17 K a further strong feature at 2.9 meV, peak VI, is observed. As it is essentially absent in the data at the lower temperatures, it is assigned to a transition from the 2.8 meV level to a level at about 5.7 meV. On the neutron energy-gain side of the data, Fig. 2(b), all corresponding anti-Stokes peaks (labeled with an additional apostrophe) are observed with the expected temperature dependence. This confirms the above assignment of the levels, also demonstrating the magnetic origin of the transitions.

The 5.0 Å neutron scattering data shown in Fig. 3 confirm the findings from the 3.8 Å measurements with higher resolution (the 2.4 K and 9.7 K data were communicated previously in Ref. 16). The 60 K spectrum provides valuable additional information. On the neutron energy-loss side, Fig. 3(a), resolved transitions are no longer observed; however, an increased inhomogeneous intensity as compared to the 2.4 K data is evident. Apparently, at 60 K, a large number of transitions with widely varying transition energies become possible, and individual transitions cannot be resolved. We interpret this as the onset of transitions into the so-called quasi-continuum in the spectrum of AFM molecular wheels.^{9,22}

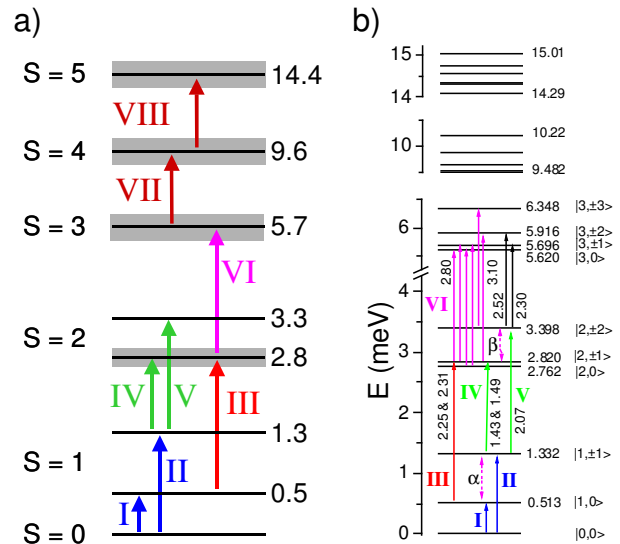


FIG. 4: (Color online) Energy spectrum of CsFe_8 as (a) derived from the neutron scattering data, and (b) calculated numerically from the microscopic Hamiltonian \hat{H} , eq. (1), using the best-fit parameters determined in this work. The level energies are given in meV. The labeling of the transitions, the classification of the levels, and the transitions α and β are discussed in the text.

In the neutron energy-gain spectrum at 60 K, Fig. 3(b), the anti-Stokes peaks I' to VI' are clearly visible, as well as two further transitions VII' and VIII' at 3.9 meV and 4.8 meV, respectively (the presence of peak VIII' will be unambiguously confirmed in Fig. 6 below). Very weak indications of peak VII' can be found in both the 3.8 Å and 5.0 Å neutron energy-gain data at 17 K. This peak is thus assigned to a transition from the excited 5.7 meV level to a further higher-lying level at about 9.6 meV. Based on the weaker intensity of peak VIII', it is assigned to a transition from the 9.6 meV level to a level at about 14.4 meV. The magnetic origin of peaks VII' and VIII', and their assignment, is less evident from the data, but is confirmed by the quantitative analysis presented in section IV.

With the above thermal-population arguments the energy spectrum as compiled in Fig. 4(a) is directly concluded from the INS measurements. For the further analysis, the following procedure was applied to each data curve on the neutron energy-loss side. The background was approximated by an analytical function and subtracted from the data. The corrected spectrum was then least-squares fitted to an appropriate number of Gaussian peaks. The decomposition into the different contributions is explicitly shown for the 3.8 Å data in Fig. 5; the fitting results for the peak positions, linewidths, and intensities are compiled in the Tables given in appendix A. The temperature variation of the peak intensities are in accord with the expected thermal Boltzmann population, supporting the above analysis.

It is interesting to inspect the linewidths provided in

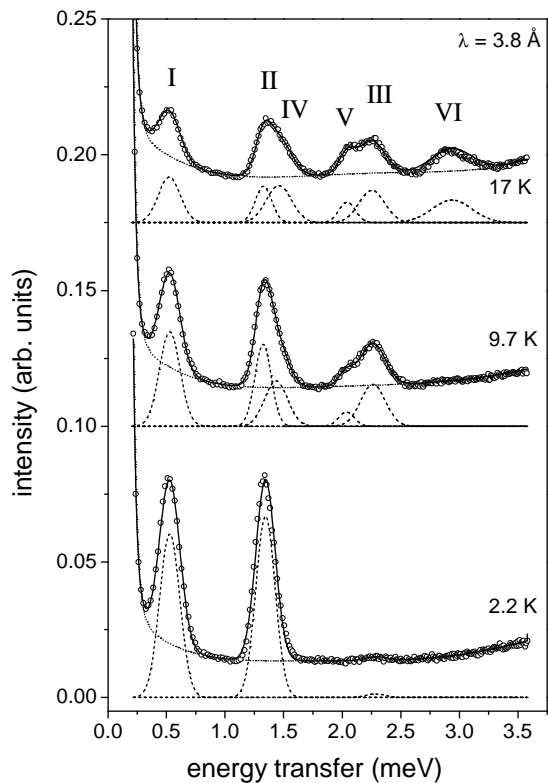


FIG. 5: Analysis of the $\lambda = 3.8 \text{ \AA}$ neutron energy-loss spectra for $T = 2.2 \text{ K}$, 9.7 K , and 17 K . The data curves for $T = 9.7 \text{ K}$ and 17 K were shifted for clarity by 0.1 and 0.175 arb. units, respectively. Open circles represent the data and solid lines fits, which included an approximated background (dotted lines) and a number of Gaussian lines (dashed lines). The parameters of the Gaussian lines are given in Table A.II.

Tables A.I and A.II. The linewidths of transitions I, II, and V are consistent with the experimental resolution for both the 3.8 \AA and 5.0 \AA data sets. This indicates that the energy levels at 0.5 meV, 1.3 meV, and 3.3 meV correspond to single states in the energy spectrum of CsFe_8 . The linewidths of transitions III and IV, which are about 0.21 meV (FWHM) for both peaks, are consistently larger than the experimental resolution. This indicates that the level at 2.8 meV in Fig. 4(a) actually relates to two (or more) close-lying states in the energy spectrum. Finally, the linewidth of transition VI, ca. 0.34 meV (FWHM), is even larger, which indicates that also the level at 5.7 meV contains two or more close-lying energy states. These findings are represented in Fig. 4(a) by the thicker gray bars.

A similar analysis was performed for the 5.0 \AA neutron energy-gain data at 60 K in an energy range which embraces peaks VI', VII', and VIII'. The decomposition of the data is shown in Fig. 6; the best-fit values for the three Gaussian lines are given in Table A.III. The inset of Fig. 6 confirms the statistical significance of peak VIII'. The observed linewidths of 0.33-0.4 meV are significantly larger than the experimental resolution, with

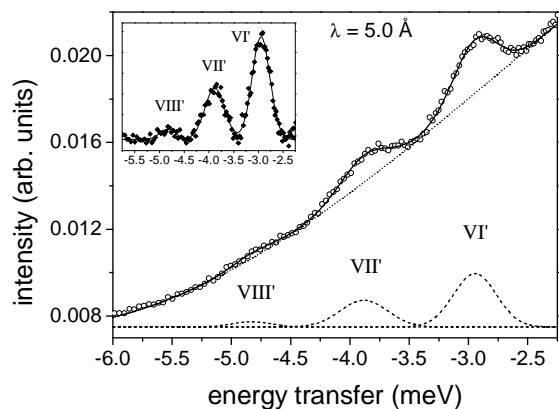


FIG. 6: Analysis of a part of the $\lambda = 5.0 \text{ \AA}$ neutron energy-gain spectra at $T = 60 \text{ K}$. Open circles represent the data and the solid line the best fit, which included an approximated background (dotted lines) and three Gaussian lines (dashed lines). The parameters of the Gaussian lines are given in Table A.III. The inset shows the data after subtraction of the background (black squares) and the three fitted Gaussian lines (solid line).

similar conclusions as for the 3.8 \AA data.

A qualitative assignment of the observed transitions is achieved by comparing the level scheme in Fig. 4(a) with the energy spectrum as calculated numerically from \hat{H} , eq. (1). In order to calculate the energy spectrum, one could use the J and D values inferred previously from high-field torque measurements.¹³ Since these values, however, are very close to the best-fit values to be determined below in section V, the energy spectrum obtained for the best-fit values, which is presented in Fig. 4(b), will be used here. In Fig. 4(b), the states are labeled by the quantum numbers S and M of the total-spin operator $\hat{S} = \sum_i \hat{S}_i$ (using the notation $|S, M\rangle$ for the levels). However, it should be stressed here that S is not a good quantum number for CsFe_8 , because of the rather large magnetic anisotropy present in the system.¹⁶ For the moment, S should be taken as an arbitrary additional label for distinguishing the energy levels; a further detailed discussion of the situation will be given in section VI.

From a comparison of Figs. 4(a) and 4(b), the identification of the experimentally observed transitions is apparent, considering the INS selection rules $\Delta S = 0, \pm 1$ and $\Delta M = 0, \pm 1$. The 0.5 meV and 1.3 meV levels correspond to transitions from the ground state $|0, 0\rangle$ to the levels $|1, 0\rangle$ and $|1, \pm 1\rangle$, respectively. As demonstrated in Ref. 16, peak I reflects the quantum tunneling of the Néel vector characterizing the low-energy spin dynamics in CsFe_8 . It was also noted that the transition between the first and second excited levels (denoted as α) is not observed, although it is formally allowed by the INS selection rules. The intensity of α is very weak compared to that of the other transitions, since the sublattice-magnetization vectors are of mesoscopic size in CsFe_8 . Peaks III, IV, and V correspond to transitions

from the $S = 1$ states to those of the $S = 2$ multiplet. Interestingly, peaks III and IV are confirmed to consist of two close transitions, in agreement with the observed enlarged linewidths (the transition $|2, \pm 1\rangle \rightarrow |2, \pm 2\rangle$, which is expected at ca. 0.6 meV at higher temperatures, turns out to be too weak in intensity to be detectable). Peak VI corresponds to transitions from the $S = 2$ states into the $S = 3$ multiplet. The zero-field-splitting of these multiplets, which allows six close transitions, is reflected by the broad linewidth of peak VI. Finally, peaks VII and VIII correspond to transitions from the $S = 3$ to the $S = 4$, and the $S = 4$ to the $S = 5$ multiplets, respectively. Here again, the spread in the transition energies of the individual transitions due to the zero-field-splitting is too small to be resolved experimentally, hence the broadened peaks.

The energy level diagram shown in Fig. 4(a) is one of the most extended level schemes determined for a molecular nanomagnet from INS measurements, yet all essential features of the data can be readily explained by basic arguments. The above analysis, in our opinion, provides a nice textbook example for the analysis of INS data from molecular clusters.

IV. EFFECTIVE HAMILTONIAN AND INELASTIC NEUTRON SCATTERING INTENSITY

In the next section a more sophisticated analysis of the data will be presented, which yields best-fit values for J and D , as well as some insight into the accuracy and limitations of the generic spin Hamiltonian (1). A fit of the data to INS spectra calculated from the microscopic Hamiltonian (1) using standard least-squares fitting routines, however, is numerically expensive for a system as large as CsFe₈. Another procedure has thus been developed, the essentials of which are outlined in this section.

In our experiments, only transitions between states of the so-called L band were observed.^{9,15,22} The L band, also known as the tower of states¹⁹ or the quasi-degenerate joint states,^{20,28} arises from a quantized rotation of the Néel vector in AFM wheels and other systems. It consists of the energetically lowest-lying states for each S , whose energies increase as $E(S) \propto S(S+1)$. This set of states can be very well described for small AFM Heisenberg rings by approximating the wave functions by $|\beta_A \beta_B S_A S_B S M\rangle$, with $S_A = S_B = 10$ for CsFe₈ (S_A and S_B denote the total spin of sublattices A and B , respectively. β_A and β_B abbreviate intermediate quantum numbers, but are omitted in the following).^{22,29} Physically, this approach works well because the internal spin structure due to the dominant Heisenberg interaction is essentially classical.^{9,15} In this approximation, the effective (two-sublattice) Hamiltonian

$$\hat{H}_{AB} = -\tilde{J} \hat{\mathbf{S}}_A \cdot \hat{\mathbf{S}}_B + \tilde{D} (\hat{S}_{A,z}^2 + \hat{S}_{B,z}^2) \quad (2)$$

with $\tilde{J} = 0.5366J$ and $\tilde{D} = 0.1870D$ is obtained for CsFe₈.²⁹ Since \hat{H}_{AB} is designed to describe only the states of the L band, numerical calculations become much cheaper (for CsFe₈, the dimension of the Hilbert space is 1679616 while that of \hat{H}_{AB} is only 441).

Concerning the energies, \hat{H}_{AB} has been demonstrated to yield very accurate results.²⁹ The calculation of INS spectra, however, needs further consideration since not only the energies but also the local transition matrix elements and so-called interference factors need to be properly approximated. While transition matrix elements are expected to be reproduced reasonably well, the situation is less obvious for the interference factors. In fact, these factors, which typically produce a pronounced oscillatory behavior of the INS scattering intensity as function of momentum transfer (Q dependence), arise from a correlation of the transition matrix elements and the geometrical structure of the molecule.^{30,31} \hat{H}_{AB} essentially replaces the octanuclear spin-5/2 ring structure of CsFe₈ by a dimer of two spin-10 centers, which is obviously a very different geometrical structure. A naive calculation of the INS spectra from \hat{H}_{AB} should thus be suspected to produce incorrect Q dependencies, and hence incorrect INS intensities. For CsFe₈ this is indeed the case. In the following, however, it will be shown that the interference effects can be retained by a suitable generalization of the INS scattering formula. The procedure is actually very simple.

For a spin cluster, the INS cross section is given by^{32,33}

$$\frac{d^2\sigma}{d\Omega d\omega} = C(Q, T) \sum_{nm} \frac{e^{-\beta E_n}}{Z(T)} I_{nm}(\mathbf{Q}) \delta(\omega - \frac{E_m - E_n}{\hbar}), \quad (3)$$

where $C(Q, T) = (\gamma e^2 / m_e c^2) (k'/k) \exp[-2W(Q, T)]$ (where all symbols have the usual meaning), $\beta = 1/(k_B T)$, and $Z(T)$ is the partition function. For a powder sample in zero magnetic field one finds³¹

$$I_{nm}(Q) = \sum_{ij} F_i^*(Q) F_j(Q) \left\{ \frac{2}{3} j_0(QR_{ij}) \tilde{\mathbf{S}}_i \cdot \tilde{\mathbf{S}}_j + j_2(QR_{ij}) \sum_q T_q^{(2)*}(\mathbf{R}_{ij}) T_q^{(2)}(\tilde{\mathbf{S}}_i \tilde{\mathbf{S}}_j) \right\}, \quad (4)$$

where $F_i(Q)$ is the magnetic form factor of the i th spin center, j_k is the spherical Bessel function of order k , and $\mathbf{R}_{ij} = \mathbf{R}_i - \mathbf{R}_j$ is the distance vector between the i th and j th ion. An explicit expression for Eq. (4) is given in Ref. 34. $T_q^{(k)}(\mathbf{v})$ is the q th component of the spherical tensor of rank k constructed from the Cartesian vector \mathbf{v} , and $T_q^{(2)}(\tilde{\mathbf{S}}_i \tilde{\mathbf{S}}_j)$ represents the tensor product $[T^{(1)}(\tilde{\mathbf{S}}_i) \otimes T^{(1)}(\tilde{\mathbf{S}}_j)]_q^{(2)}$. The ordered products $\tilde{S}_{i\alpha} \tilde{S}_{j\beta}$, which appear in the explicit expression of $T_q^{(2)}(\tilde{\mathbf{S}}_i \tilde{\mathbf{S}}_j)$, stand for $\langle n | \hat{S}_{i\alpha} | m \rangle \langle m | \hat{S}_{j\beta} | n \rangle$, where $|n\rangle$ denotes an eigenstate of the Hamiltonian under consideration. Equation (4) can be also written more compactly

as

$$I_{nm}(Q) = \sum_{ij} \sum_{kq} f_{ij}^{kq}(Q, \mathbf{R}_{ij}) U_q^{(k)}(\tilde{\mathbf{S}}_i, \tilde{\mathbf{S}}_j), \quad (5)$$

whereby introducing the interference factors $f_{ij}^{kq}(Q, \mathbf{R}_{ij})$ ($k = 0, 2$ and $|q| \leq k$) and the symmetrized spherical tensors $U_q^{(k)}$ (which are proportional to $\text{Re}[T_q^{(k)}]$ for $q \geq 0$ and $\text{Im}[T_q^{(k)}]$ for $q < 0$, see appendix B).

The easiest way to derive an effective formula for the INS intensity is to follow the procedure suggested in Ref. 35 for the construction of an effective Hamiltonian for AFM spin clusters with essentially classical internal spin structure. It starts by noting that a classical spin structure relates to a mean-field situation for each of the AFM sublattices. Accordingly, all spins $\hat{\mathbf{S}}_i$ on a sublattice ν are replaced by the mean-field spin $\tilde{\mathbf{S}}_\nu/N_\nu$, where $\tilde{\mathbf{S}}_\nu = \sum_{i \in \nu} \hat{\mathbf{S}}_i$ and N_ν is the number of spins on sublattice ν .

Concerning the INS intensity, one replaces all matrix elements $\tilde{S}_{i\alpha}$ with $i \in \nu$ by $\tilde{S}_{\nu\alpha}/N_\nu$, puts all $\tilde{S}_{\nu\alpha}$ outside the brackets, and immediately obtains

$$I_{nm}(Q) = \sum_{\nu\mu} \sum_{kq} \bar{f}_{\nu\mu}^{kq}(Q) U_q^{(k)}(\tilde{\mathbf{S}}_\nu, \tilde{\mathbf{S}}_\mu) \quad (6)$$

with the effective interference factors

$$\bar{f}_{\nu\mu}^{kq}(Q) = \frac{1}{N_\nu N_\mu} \sum_{i \in \nu, j \in \mu} f_{ij}^{kq}(Q, \mathbf{R}_{ij}). \quad (7)$$

In the case of CsFe₈, with its two sublattices A and B , Eq. (6) yields a scattering formula analogous to that of a dimer, but with the dimer interference factors $f_{11}(Q)$ and $f_{12}(Q)$ replaced by the effective interference factors $\bar{f}_{AA}(Q)$ and $\bar{f}_{AB}(Q)$. In the scattering formula, now only the matrix elements $\tilde{S}_{A\alpha}$ and $\tilde{S}_{B\alpha}$ appear, which can be calculated from the eigenpairs obtained from \hat{H}_{AB} .

Figure 7 presents numerical results for the Q dependence of the INS intensity in CsFe₈ as calculated from the microscopic spin Hamiltonian \hat{H} (solid lines), the effective spin Hamiltonian \hat{H}_{AB} (dotted lines), and the effective Hamiltonian \hat{H}_{AB} but now using Eq. (6) for the INS intensity (dashed lines) [in the first two cases Eq. (4) was used]. Noting Fig. 7 it is clear that the pure dimer model is not capable of producing correct Q dependencies. This is not surprising, and just reflects the fact that a dimer model can only describe the interference between two ions, while in the full cluster interference occurs between eight ions. This also explains why the exact Q dependence shows more oscillations per Q range. In contrast, the above procedure of reinstating the full geometrical structure of the molecule works very well. For the intra-multiplet transition α ($|1, 0\rangle \rightarrow |1, \pm 1\rangle$), the exact and effective dimer curves are essentially indistinguishable in Fig. 7(c). The curves in Figs. 7(a) and (b) also coincide with each other if one scales the effective dimer curves by factors of 0.940 and 0.911, respectively. These

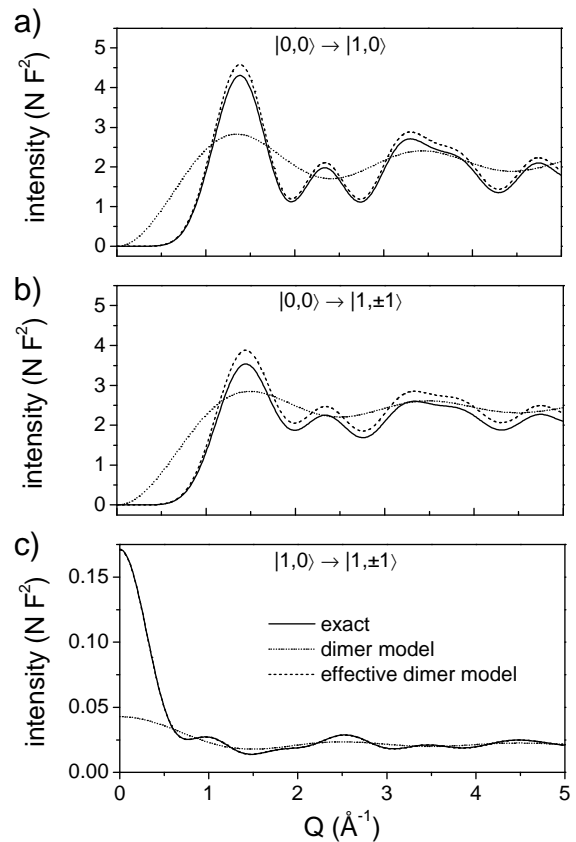


FIG. 7: Q dependence of the neutron scattering intensity of CsFe₈ as calculated from the full Hamiltonian (1) (solid lines), the dimer Hamiltonian \hat{H}_{AB} (dotted lines), and the dimer Hamiltonian \hat{H}_{AB} using the effective INS formula Eq. (6) (dashed lines). Results are shown for the three transitions (a) $|0, 0\rangle \rightarrow |1, 0\rangle$, (b) $|0, 0\rangle \rightarrow |1, \pm 1\rangle$, and (c) $|1, 0\rangle \rightarrow |1, \pm 1\rangle$, see Fig. 4. In the calculations with the pure dimer model, the distance between the two spins S_A and S_B was set to 3.2 Å, corresponding to the iron-iron distance in CsFe₈.

numbers also give an idea of the accuracy of the transition matrix elements obtained from the effective Hamiltonian approach, which apparently is better than 10%. Furthermore, Fig. 7 clearly shows that for $Q > 0.5$ Å⁻¹ the intensity of the intra-spin-multiplet transition α is indeed two orders of magnitude weaker than that of transitions I and II as noted previously.¹⁶

V. QUANTITATIVE ANALYSIS

In this section a complete quantitative analysis of the experimental data is provided. Typically, spin-Hamiltonian parameters are obtained by least-square fitting the calculated energies (or transition energies) to the peak positions obtained from a Gaussian analysis of the data, similar to that shown in Fig. 5. However, since in the present case some of the observed peaks are composed of several individual but close-lying transitions the

experimental spectra were fitted directly by simulated INS spectra.

Only the results of the analysis for the 3.8 Å neutron energy-loss data at 17 K will be shown explicitly, as this data set contains the most information and thus allows the best judgment as to the agreement between experiment and theory. A similar analysis for the other data yields redundant results. For each pair of values for J and D , theoretical INS spectra were calculated from the eigenpairs of \hat{H}_{AB} using the effective INS formula Eq. (5). For the final best-fit values, and some other cases, spectra were calculated from the microscopic spin Hamiltonian \hat{H} , using Eq. (4), in order to confirm the accuracy of the results. In the calculations, the crystallographic positions of the iron(III) ions were used, and the form factors $F_i(Q)$ were estimated by the standard analytical approximations.³⁶ The variation of the Q range with energy transfer $\hbar\omega$ of the IN5 spectrometer was accounted for by numerically integrating $I(\omega, Q)$, where $Q \equiv Q(\omega, \theta)$, over the scattering angle spanned by the detectors. $Q(\omega, \theta)$ is related to the energy transfer $\hbar\omega$ and the angle θ of the scattered neutron beam via the scattering triangle.

The result of a least-squares fit to the 3.8 Å, 17 K neutron energy-loss data is shown in Fig. 8(a). The agreement is excellent, with the calculated curve reproducing all the details present in the data. The obtained best-fit parameters were $J = -1.80(2)$ meV and $D = -0.050(1)$ meV, which are in agreement with previous findings.^{13,16} The linewidth was set as a free parameter in the fit, yielding 0.18 meV, very close to the nominal instrumental resolution of 0.161 meV. The good agreement between experimental and calculated curves is also notable because several transitions contribute to the various peaks, as indicated by the vertical solid lines in Fig. 8(a). Peaks I, II, and V correspond to individual transitions, while peaks III and IV are each made up of two close-lying transitions, and peak VI is the result of six close-lying transitions, in perfect agreement with the conclusions drawn from the analysis of the linewidths in section III [see also Fig. 4(a)]. The explicit assignment of all the transitions which form the spectrum in Fig. 8 is given in Ref. 37. From the expected transitions between the $S = 0, 1, 2,$ and 3 multiplets, all but two are observed. These are the two intra-multiplet transitions $|2, \pm 1\rangle \rightarrow |2, \pm 2\rangle$ and $|1, 0\rangle \rightarrow |1, \pm 1\rangle$ expected at 0.571 meV and 0.818 meV, respectively. Their intensity is two orders of magnitude weaker as compared to the other transitions, because, as mentioned already and discussed in Ref. 16, the sublattice-magnetization vectors are of mesoscopic size in CsFe₈. The other intra-multiplet transitions, while allowed, occur at too low energy and are thus buried under the elastic line.

Using the best-fit parameters, the transitions between the $S = 3, 4,$ and 5 multiplets can also be calculated. The result agrees nicely with the peak positions of peaks VII and VIII, thus confirming their magnetic origin, and their assignment as transitions from the $S = 3$ to $S = 4$

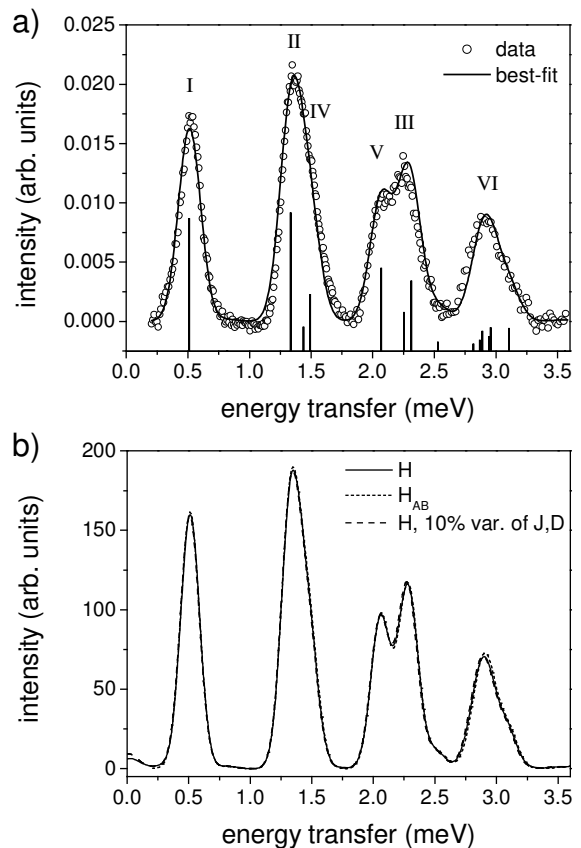


FIG. 8: (a) Best-fit curve, to the background-subtracted data, for the $\lambda = 3.8$ Å neutron energy-loss spectrum for $T = 17$ K ($J = -1.80$ meV, $D = -0.050$ meV). The vertical lines indicate the transitions and their intensities which contribute to the neutron spectrum. (b) Calculated neutron energy-loss spectra. The solid curve was calculated with the best-fit parameters using the effective Hamiltonian approach, Eq. (6), the short-dashed curve was calculated with the best-fit parameters using the full Hamiltonian, Eq. (4), and the dashed curve was calculated from the full Hamiltonian with a 10% distribution in J and D (see text for details).

and $S = 4$ to $S = 5$ multiplets, respectively.

As a summary of the analysis so far, the transitions between the $S = 0, 1, 2, 3, 4,$ and 5 multiplets (of the L band) were observed and could be reproduced very well by the Hamiltonian \hat{H} . Apparently, the generic Hamiltonian \hat{H} , which contains only the two free parameters J and D , provides an excellent description of the excitations in CsFe₈, within the experimental resolution of the present experiments of about 0.1 meV.

Indications have been found in previous works on other AFM wheels that Hamiltonian (1), though being an excellent approximation, is not complete and needs to be extended by further weak terms.^{11,14,17,38,39,40} This raises the question as to how well Hamiltonian (1) in fact describes CsFe₈. It should be noted that for some wheels, effects which are due to coupling of the spin system to the environment have been found,^{40,41} however these are

a different subject and not of interest here. The presence of further weak terms seems particularly relevant for CsFe₈ as it does not exhibit eight-fold symmetry; the molecule investigated in this work has a crystallographic C_2 axis. Accordingly, two deviations from the perfect situation described by Hamiltonian (1) were considered, i) an additional biaxial anisotropy term and ii) a variation of the exchange and anisotropy constants along the ring.

Biaxial anisotropy contributions for rather symmetric wheels were recently deduced for the Cr₈ and the Fe₁₀ wheels.^{17,39} In these cases, the microscopic Hamiltonian $\hat{H}_1 = \hat{H} + E \sum_i (\hat{S}_{i,x}^2 - \hat{S}_{i,y}^2)$ was used. The Cr₈ wheel exhibits a crystallographic C_4 symmetry (though indications of a structural phase transition at low temperatures seem to have been found), however the INS data were significantly better described with $|E| = 0.004(1)$ meV, corresponding to a ratio $|E/D| = 0.11$.³⁹ For the Fe₁₀ wheel, which exhibits crystallographic C_2 symmetry, $|E| = 0.0036(2)$ meV was found, corresponding to a quite substantial ratio $|E/D| = 0.21$.¹⁷

In the case of CsFe₈, an upper limit for the value of $|E|$ can be inferred from the present data as follows. A biaxial anisotropy would split the two $|1, \pm 1\rangle$ levels, which are degenerate in a uniaxial model. Accordingly peak II should split into two [see also Fig. 4(a)]. The 5.0 Å data at low temperatures yields a linewidth for peak II of ca. 0.13 meV (see Table A.II), very close to the nominal experimental resolution. Thus, a splitting of, for example, 0.08 meV (corresponding to an estimated linewidth of peak II of ca. 0.18 meV) would have been clearly detected in this experiment. Since the splitting of the $|1, 0\rangle$ and $|1, \pm 1\rangle$ levels by the D term is ca. 0.8 meV, one thus can conclude that $|E/D| < 0.1$, or with the determined value for D that $|E| < 0.005$ meV. For a more quantitative analysis, the 3.8 Å, 17 K neutron energy-loss data was least-squares fitted to the effective-Hamiltonian version of \hat{H}_1 , with J , D , and E (and the linewidth) as free parameters. Independent of the starting values, the fit converged to the same values for J and D as above, and to $|E| < 5 \times 10^{-5}$ meV, that is, values which are zero within the statistical error. The inclusion of a biaxial term thus did not improve the quality of the fit.

A more suitable technique for detecting a possible E term, or other additional terms in the Hamiltonian, is electron paramagnetic resonance (EPR), as it allows one to detect the transitions within a spin multiplet with higher resolution (in the case of CsFe₈ this is ca. 0.01 meV compared to ca. 0.1 meV for the INS experiment). EPR experiments at 35 GHz and 190 GHz on single-crystals of CsFe₈ were thus performed (and will be reported elsewhere⁴²). The EPR spectra are well described using only uniaxial anisotropy, which sets a rather stringent upper limit on the strength of a biaxial anisotropy. Thus from a magnetic perspective CsFe₈ is a very uniaxial and symmetric wheel.

As a second possible deviation from the generic situation, a variation of the exchange and anisotropy constant within the ring was considered, as described by the

Hamiltonian $\hat{H}_2 = -\sum_i J_i \hat{\mathbf{S}}_i \cdot \hat{\mathbf{S}}_{i+1} + \sum_i D_i \hat{S}_{i,z}^2$ (there enforcing $\sum_i J_i = J$ and $\sum_i D_i = D$). A variation might originate, for instance, from the reduced C_2 symmetry of the ring, which gives rise to four slightly different Fe-Fe distances, or from disorder in the crystallites. In order to test such an effect, J_i and D_i values were drawn from a Gaussian distribution with a 10% standard deviation, and the INS spectra calculated. This is shown in Fig. 8(b), and is compared to the calculation for the generic Hamiltonian (1) [Fig. 8(b) also presents the INS spectrum as calculated with the effective Hamiltonian approach, just to reinforce the high accuracy of this procedure]. It is apparent that a 10% variation of the parameters is quite possible within the present experiments. This is not unexpected because, as discussed in Ref. 13, a change of the coupling and anisotropy parameters along the ring has no effect on the energies of the states of the L band up to first order. However, this is not so for the states of the E band, which correspond to the quantized spin-wave excitations on the ring.^{15,22} Observation of the spin waves in CsFe₈, expected at around 7.5 meV and 10 meV at low temperatures, could thus allow further insight into this issue.

VI. DISCUSSION

In the previous sections it has been shown that the generic Hamiltonian \hat{H} , Eq. (1), which involves only the two parameters J and D , provides an excellent description of a significant portion of the low-lying excitations in CsFe₈. In the analysis, the states were labeled by the spin quantum number S , which, however, since D is non-zero, is not an exact quantum number (though M still is). The question thus arises as to how good a quantum number S is. The situation for CsFe₈ is in fact quite ambivalent.

In our previous INS study¹⁶ it has been demonstrated that the lowest energy transition $|0, 0\rangle \rightarrow |1, 0\rangle$, or peak I, corresponds to the Néel-vector tunneling transition. Here, the influence of the magnetic anisotropy is so strong that S completely loses its significance as a quantum number for the two involved states. The label S only can be used in the sense that the states are connected adiabatically to the corresponding states at zero magnetic anisotropy. This is visible in Fig. 9, which presents the calculated energy spectrum as function of the ratio D/J (using $J = -1.80$ meV). For small D/J the states obviously can be labeled by S and M ("small" means here $D/J < 0.02$, Ref. 23). For large D/J , where S certainly is no longer a good quantum number, every state nevertheless can be uniquely related back to one of the $|S, M\rangle$ states at small D/J . Hence S can still be used as a label, although the actual wave functions by no means are reasonably approximated by eigenfunctions of $\hat{\mathbf{S}}^2$.

The loss of the significance of S with increasing D/J can be inferred from the energy spectrum, Fig. 9, at least qualitatively (for a more rigorous discussion one would

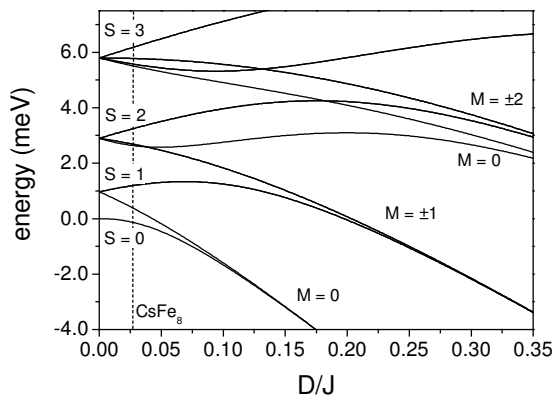


FIG. 9: Low-lying energy spectrum of an octanuclear $s = 5/2$ wheel as function of D/J , as calculated from \hat{H} with $J = -1.80$ meV. At small anisotropies, the levels can be classified by the spin quantum numbers S and M . For large anisotropies, S loses its significance, though M remains an exact quantum number. The dashed line indicates the parameter D/J as obtained for CsFe_8 .

have to inspect the wave functions, but here a qualitative consideration shall suffice). For $D/J = 0$, the levels $|S, \pm M\rangle$ are degenerate since S is an exact quantum number. For small values of D/J the levels split, but the states corresponding to a particular S are still clustered together. For large D/J , however, the pattern of the level clustering changes completely. For instance, at small D/J the gap between the $S = 0$ ground state and the two $S = 1$ levels is much larger than the splitting between the two $S = 1$ levels. This indicates that S is a good quantum number and that the three states $|0, 0\rangle$, $|1, 0\rangle$, and $|1, \pm 1\rangle$ are approximately eigenfunctions of \hat{S}^2 . For larger D/J , however, the two states $|0, 0\rangle$ and $|1, 0\rangle$ come close to each other, while $|1, \pm 1\rangle$ splits off and joins the $|2, \pm 1\rangle$ level. In this situation the wave functions are clearly no longer eigenfunctions of \hat{S}^2 .

It is interesting to note in Fig. 9 that the value of D/J for this crossover apparently increases with the energies of the spin states. Concerning the states of the $S = 0$ and $S = 1$ multiplets, the crossover is at about $D/J = 0.02$.²³ At this value, however, the states of the next-higher lying $S = 2$ multiplet (and the multiplets with $S > 2$) are still clustered together; only at significantly higher D/J values are these levels split so strongly that they start to join levels coming from other spin multiplets (the $|2, \pm 1\rangle$ level approaches the $|1, \pm 1\rangle$ level of the $S = 1$ multiplet, and $|2, 0\rangle$ and $|2, \pm 2\rangle$ merge with levels of the $S = 3$ multiplet). From Fig. 9 it can thus be seen that with increasing magnetic anisotropy D/J the levels successively lose their S character, with larger crossover- D/J values for larger S .

This provides a rather intuitive picture of the Néel vector dynamics in AFM wheels. The situation at zero magnetic anisotropy has been well discussed in previous works:^{9,15,19,20,22,28} The lowest-lying excitations, which form the L band, may be characterized as a quantized

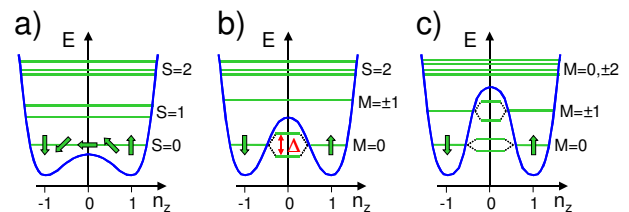


FIG. 10: (Color online) Qualitative sketch of the semiclassical picture for the dynamics of the Néel vector in AFM wheels. (a) Small magnetic anisotropy, where the dynamics is characterized by rotation of the Néel vector, (b) magnetic anisotropy exceeding $S_0/\hbar > 4$, where the low-energy dynamics is characterized by a tunneling of the Néel vector, and (c) larger magnetic anisotropy, where successively further higher-lying states are driven into the tunneling regime.

rotation of the Néel vector (that is, in a classical picture the Néel vector may precess freely).

The introduction of an easy-axis anisotropy means that (in a classical picture) the orientations of the Néel vector along the anisotropy axis (z axis) are energetically favored over the other orientations, which is usually sketched by a double-well potential with two minima for the Néel vector along the z axis, and an energy barrier in between (see Fig. 10). For small anisotropies the energy barrier is small and the precession of the Néel vector is largely undisturbed [Fig. 10(a)], and thus may be observed as for instance in the molecule Cr_8 .¹⁵ With increasing anisotropy the energy barrier increases, so that the (classical) ground state eventually falls below the top of the barrier, and the dynamics is characterized by tunneling of the Néel vector, Fig. 10(b).^{24,25,26} In the quantum mechanical picture, this affects the $S = 0$ and $S = 1$ multiplets, which lose their S character. For the higher-lying multiplets, the anisotropy is not yet strong enough to compete with the higher rotational energies involved in these states (as indicated by their larger S values), so that they are still well characterized by a rotation of the Néel vector, and by S . With further increasing anisotropy, the two lowest-lying states are driven deeper into the tunneling regime (as indicated in Fig. 9 by the exponentially shrinking gap between $|0, 0\rangle$ and $|1, 0\rangle$), but eventually also the next-higher levels become tunneling states (as indicated in Fig. 9 by the exponentially shrinking gap between $|1, \pm 1\rangle$ and $|2, \pm 1\rangle$), see Fig. 10(c). This continues with further increasing anisotropy.

Apparently for CsFe_8 , the situation portrayed in Fig. 10(b) is realized, where the low-energy dynamics is characterized by a tunneling of the Néel vector (and the quantum number S has lost its meaning), while at the higher energies the dynamics can still be rationalized as a rotation of the Néel vector (so that the spin multiplets with $S \geq 2$ retain their S character). The $S = 2$ multiplet nevertheless shows an interesting signature of the strong anisotropy, namely the $|2, 0\rangle$ and $|2, \pm 1\rangle$ levels are very close to each other in CsFe_8 (see Fig. 9). This indicates a strong fourth-order term B_4^0 for the $S = 2$ multiplet with

a ratio $B_4^0/D_2 = 5 \times 10^{-4}$ (for comparison in Mn_{12}).⁴³
 $B_4^0/D_2 = 5 \times 10^{-5}$).⁴⁴

VII. CONCLUSIONS

In this work the previous INS measurements¹⁶ on the AFM wheel CsFe_8 were extended to a larger temperature and energy transfer range. This has allowed us to observe the L -band states from the ground state up to the $S = 5$ multiplet. The analysis of the data, on a qualitative level, was straight forward and of textbook quality. For the quantitative analysis the effective Hamiltonian concept, which is well-known to be very successful in the interpretation of energy spectra, was extended such as to also facilitate an accurate calculation of the INS scattering intensities. This allowed a least-squares fitting of the data. The results showed that the low-energy magnetism in the CsFe_8 wheel is excellently described by the generic spin Hamiltonian \hat{H} , Eq. (1), with only two magnetic parameters. The role of the quantum number S has also been discussed qualitatively, and showed that in CsFe_8 the situation is ambivalent: On the one hand, the very-lowest excitations are characterized by a tunneling of the Néel vector, implying that S is no longer a good quantum number, while on the other hand the higher-lying states are still well described as rotational modes of the Néel vector, for which S is a good quantum number.

It would be clearly interesting to synthesize and identify AFM wheels with an anisotropy so strong that the situation of Fig. 10(c) is realized, i.e., where also higher-lying states are driven into a tunneling regime. The semi-classical theory for such a situation has not been, to the best of our knowledge, yet developed. It would be, however, important to put the qualitative picture of the Néel-vector dynamics in strongly anisotropic wheels outlined in section VI on a sound theoretical basis.

For very large D/J , the situation should bear a close analogy to that found in the $(\text{Mn}_4)_2$ molecule, which represents a dimer of two Mn_4 single-molecule magnets coupled by a weak AFM interaction.^{46,47,48} This molecule attracted quite some interest recently because of its distinct magnetic hysteresis curve. According to the effective two-sublattice Hamiltonian \hat{H}_{AB} , Eq. (2), an AFM wheel can be considered magnetically as a dimer of two large spins S_A and S_B . Thus, for small J , and because of the easy-axis anisotropies of the spins S_A and S_B , one formally would have exactly the situation of a dimer of single-molecule magnets with a weak AFM interaction, similarly as in $(\text{Mn}_4)_2$. It is thus predicted that in highly anisotropic AFM wheels phenomena such as exchange-biased magnetic hysteresis curves could be observable.

Acknowledgments

Financial support by the Swiss National Science Foundation and the European Union (EC-RTN-

QUEMOLNA, Contract No. MRTN-CT-2003-504880) is gratefully acknowledged.

APPENDIX A

As described in section III, the experimental INS spectra were analyzed by approximating the background with an analytical function and least-square fitting of the corrected data to an appropriate number of Gaussian lines. The resulting parameters for the six peaks I to VI visible in the 3.8 Å energy-loss spectra [Figs. 2(a) and 5] are listed in Table A.I, those for the peaks I, II, and IV visible in the 5.0 Å energy-loss spectra [Fig. 3(a)] are listed in Table A.II, and those for the three peaks VI' to VIII' visible in the 3.8 Å energy-gain spectra at $T = 60$ K [Figs. 3(b) and 6] are listed in Table A.III. The results of a similar analysis for the other neutron energy-gain data, while in agreement, is not given here because of redundancy. The linewidths reported in the tables are the widths of the best-fit Gaussian lines (no convolution with instrumental resolution). For comparison, also the theoretically expected instrumental resolutions of IN5 are given in the last columns. These, however, are not achieved in the experiment (probably due to sample inhomogeneity). This is evident from the experimental resolution at the elastic line, which for $\lambda = 5.0$ Å (3.8 Å) was 121 μeV (161 μeV) as compared to the theoretical instrumental resolution of 105 μeV (141 μeV). Hence, for

TABLE I: Results of the analysis of the $\lambda = 3.8$ Å neutron energy-loss spectra for the temperatures 2.2 K, 9.7 K, and 17 K. Each peak in the data was least-square fitted by a Gaussian line; the peak position, linewidth (FWHM), and intensity (in arb. units) are listed below. For further details of the analysis see section III and Fig. 5. The last column reports the theoretically estimated instrumental resolution of IN5 at the respective transfer energies.

peak	T	peak energy (meV)	width (meV)	intensity ($\times 10^{-2}$ a.u.)	instr. width (meV)
I	2.2 K	0.5274(3)	0.1732(8)	1.31(1)	0.132
	9.7 K	0.5275(4)	0.1747(9)	0.761(4)	0.132
	17 K	0.5237(8)	0.186(2)	0.393(3)	0.132
II	2.2 K	1.3450(3)	0.1647(6)	1.382(5)	0.119
	9.7 K	1.324(3)	0.141(5)	0.5(1)	0.119
	17 K	1.327(4)	0.140(7)	0.24(5)	0.119
III	2.2 K	2.289(9)	0.17(2)	0.029(3)	0.105
	9.7 K	2.263(2)	0.210(4)	0.41(1)	0.106
	17 K	2.253(4)	0.221(6)	0.33(1)	0.106
IV	9.7 K	1.43(2)	0.20(2)	0.4(1)	0.118
	17 K	1.46(2)	0.22(1)	0.37(5)	0.117
V	9.7 K	2.036(4)	0.134(6)	0.09(1)	0.109
	17 K	2.042(3)	0.140(4)	0.13(1)	0.109
VI	17 K	2.937(2)	0.338(3)	0.354	0.097

TABLE II: Results of the analysis of the $\lambda = 5.0 \text{ \AA}$ neutron energy-loss spectra for the temperatures 2.4 K, 9.7 K, and 17 K. Each peak in the data was least-square fitted by a Gaussian line; the peak position, linewidth (FWHM), and intensity (in arb. units) are listed below. For further details of the analysis see section III. The last column reports the theoretically estimated instrumental resolution of IN5 at the respective transfer energies.

peak	T	peak energy (meV)	width (meV)	intensity ($\times 10^{-2}$ a.u.)	instr. width (meV)
I	2.4 K	0.5178(5)	0.133(1)	2.53(2)	0.094
	9.7 K	0.5211(2)	0.1255(4)	1.361(5)	0.094
	17 K	0.5203(5)	0.12(1)	0.66(1)	0.094
II	2.4 K	1.3171(4)	0.1303(8)	2.41(1)	0.080
	9.7 K	1.3040(5)	0.110(2)	0.84(4)	0.080
	17 K	1.303(1)	0.101(4)	0.30(3)	0.080
IV	9.7 K	1.398(5)	0.184(4)	0.86(4)	0.079
	17 K	1.420(5)	0.208(5)	0.80(3)	0.078

TABLE III: Results of the analysis of the $\lambda = 5.0 \text{ \AA}$ neutron energy-gain spectra at $T = 60 \text{ K}$. Each peak in the data was least-square fitted by a Gaussian line. The peak position, linewidth (FWHM), and intensity (in arb. units) are listed below. For further details of the analysis see sections III and IV, and Fig. 6. The last column reports the theoretically estimated instrumental resolution of IN5 at the respective transfer energies.

peak	peak energy (meV)	width (meV)	intensity ($\times 10^{-2}$ a.u.)	instr. width (meV)
VI'	-2.945(4)	0.363(8)	0.112(3)	0.187
VII'	-3.883(8)	0.400(2)	0.062(3)	0.218
VIII'	-4.83(4)	0.33(9)	0.010(3)	0.252

the neutron energy-loss side the experimental resolution should be assumed to be essentially independent on energy transfer and of the value at the elastic line. The errors in the tables are the statistical errors returned by the fitting routine. For a complete error analysis instrumental uncertainties (widths of time channels, inaccurate sample position, etc.), which amount to a few μeV , also have to be considered.

For a given peak, the best-fit values for the transition energies obtained from the various curves show some variation, however, this is well within the typical limits. For transition II, the obtained linewidths at the higher

temperatures, see Tables A.I and A.II, are unrealistically small, however, this is not significant in view of the close proximity of transitions II and IV.

APPENDIX B

In this appendix, explicit expressions for the symmetrized spherical tensors $U_q^{(k)}$ and the interference factors f_{ij}^{kq} are given, which were introduced via Eq. (6) in section IV in order to provide a compact notation for the INS scattering intensity of powder samples. The symmetrized spherical tensors read

$$\begin{aligned}
U_0^{(0)}(\tilde{\mathbf{S}}_i \tilde{\mathbf{S}}_j) &= \tilde{S}_{ix} \tilde{S}_{jx} + \tilde{S}_{iy} \tilde{S}_{jy} + \tilde{S}_{iz} \tilde{S}_{jz}, \\
U_0^{(2)}(\tilde{\mathbf{S}}_i \tilde{\mathbf{S}}_j) &= (2\tilde{S}_{iz} \tilde{S}_{jz} - \tilde{S}_{ix} \tilde{S}_{jx} - \tilde{S}_{iy} \tilde{S}_{jy}) / \sqrt{6}, \\
U_2^{(2)}(\tilde{\mathbf{S}}_i \tilde{\mathbf{S}}_j) &= (\tilde{S}_{ix} \tilde{S}_{jx} - \tilde{S}_{iy} \tilde{S}_{jy}) / \sqrt{2}, \\
U_{-2}^{(2)}(\tilde{\mathbf{S}}_i \tilde{\mathbf{S}}_j) &= \tilde{S}_{ix} \tilde{S}_{jy} + \tilde{S}_{iy} \tilde{S}_{jx}, \\
U_1^{(2)}(\tilde{\mathbf{S}}_i \tilde{\mathbf{S}}_j) &= \tilde{S}_{ix} \tilde{S}_{jz} + \tilde{S}_{iz} \tilde{S}_{jx}, \\
U_{-1}^{(2)}(\tilde{\mathbf{S}}_i \tilde{\mathbf{S}}_j) &= \tilde{S}_{iy} \tilde{S}_{jz} + \tilde{S}_{iz} \tilde{S}_{jy},
\end{aligned} \tag{B1}$$

and the corresponding interference factors

$$\begin{aligned}
f_{ij}^{00}(Q, \mathbf{R}_{ij}) &= F_i^* F_j \frac{2}{3} j_0(QR_{ij}), \\
f_{ij}^{20}(Q, \mathbf{R}_{ij}) &= F_i^* F_j j_2(QR_{ij}) \frac{3R_{ij,z}^2 - R_{ij}^2}{\sqrt{6}R_{ij}^2}, \\
f_{ij}^{22}(Q, \mathbf{R}_{ij}) &= F_i^* F_j j_2(QR_{ij}) \frac{R_{ij,x}^2 - R_{ij,y}^2}{\sqrt{2}R_{ij}^2}, \\
f_{ij}^{2-2}(Q, \mathbf{R}_{ij}) &= F_i^* F_j j_2(QR_{ij}) \frac{R_{ij,x} R_{ij,y}}{R_{ij}^2}, \\
f_{ij}^{21}(Q, \mathbf{R}_{ij}) &= F_i^* F_j j_2(QR_{ij}) \frac{R_{ij,x} R_{ij,z}}{R_{ij}^2}, \\
f_{ij}^{2-1}(Q, \mathbf{R}_{ij}) &= F_i^* F_j j_2(QR_{ij}) \frac{R_{ij,y} R_{ij,z}}{R_{ij}^2}.
\end{aligned} \tag{B2}$$

In the previous literature, the form factors $F_i(Q)$ were not included in the definition of the interference factors, which is physically sound, as these two factors have different physical origins. Here, however, they were included in the f_{ij}^{kq} terms, because the approach described in section IV for the calculation of the INS intensity, from an effective Hamiltonian, is also very useful in the case of heteronuclear systems (such as the single-molecule magnet Mn_4Br , Ref. 48). In these cases the equations simplify considerably in the chosen notation.

* Corresponding author.

E-mail: waldmann@iac.unibe.ch

¹ R. Sessoli, D. Gatteschi, A. Caneschi, and M. A. Novak, Nature (London) **365**, 141 (1993).

² J. R. Friedman, M. P. Sarachik, J. Tejada, and R. Ziolo,

Phys. Rev. Lett. **76**, 3830 (1996).

³ L. Thomas, F. Lioni, R. Ballou, D. Gatteschi, R. Sessoli, and B. Barbara, Nature (London) **383**, 145 (1996).

⁴ W. Wernsdorfer and R. Sessoli, Science **284**, 133 (1999).

⁵ D. Gatteschi and R. Sessoli, Angew. Chem. Int. Ed. **42**,

- 268 (2003).
- ⁶ K. L. Taft, C. D. Delfs, G. C. Papaefthymiou, S. Foner, D. Gatteschi, and S. J. Lippard, *J. Am. Chem. Soc.* **116**, 823 (1994).
 - ⁷ D. Gatteschi, A. Caneschi, L. Pardi, and R. Sessoli, *Science* **265**, 1054 (1994).
 - ⁸ E. J. L. McInnes, S. Piligkos, G. A. Timco, and R. E. P. Winpenny, *Coordin. Chem. Rev.* **249**, 2577 (2005).
 - ⁹ O. Waldmann, *Coordin. Chem. Rev.* **249**, 2550 (2005).
 - ¹⁰ A. Cornia, M. Affronte, A. G. M. Jansen, G. L. Abbati, and D. Gatteschi, *Angew. Chem. Int. Ed. Engl.* **38**, 2264 (1999).
 - ¹¹ A. Cornia, A. G. M. Jansen, and M. Affronte, *Phys. Rev. B* **60**, 12177 (1999).
 - ¹² O. Waldmann, J. Schülein, R. Koch, P. Müller, I. Bernt, R. W. Saalfrank, H. P. Andres, H. U. Güdel, and P. Alenspach, *Inorg. Chem.* **38**, 5879 (1999).
 - ¹³ O. Waldmann, R. Koch, S. Schromm, J. Schülein, P. Müller, I. Bernt, R. W. Saalfrank, F. Hampel, and E. Balthes, *Inorg. Chem.* **40**, 2986 (2001).
 - ¹⁴ M. Affronte, A. Cornia, A. Lascialfari, F. Borsa, D. Gatteschi, J. Hinderer, M. Horvatic, A. G. M. Jansen, and M. H. Julien, *Phys. Rev. Lett.* **88**, 167201 (2002).
 - ¹⁵ O. Waldmann, T. Guidi, S. Carretta, C. Mondelli, and A. L. Dearden, *Phys. Rev. Lett.* **91**, 237202 (2003).
 - ¹⁶ O. Waldmann, C. Dobe, H. Mutka, A. Furrer, and H. U. Güdel, *Phys. Rev. Lett.* **95**, 057202 (2005).
 - ¹⁷ P. Santini, S. Carretta, G. Amoretti, T. Guidi, R. Caciuffo, A. Caneschi, D. Rovai, Y. Qiu, and J. R. D. Copley, *Phys. Rev. B* **71**, 184405 (2005).
 - ¹⁸ Dipole-dipole interactions, which add a term $\sum_{i \neq j} \hat{\mathbf{S}}_i \cdot \mathbf{D}_{ij}^{dip} \cdot \hat{\mathbf{S}}_j$ to Hamiltonian (1), cannot be neglected in general. However, as long as one is concerned only with the lowest lying states, as in the present work, their effects can be lumped into a single-ion term $\sum_i \hat{S}_{i,z}^2$, that is, the anisotropy parameter D should be understood in this work as to parameterize both the dipole-dipole and ligand-field interactions. This approach is very convenient for physical considerations where the actual origin of the anisotropy is not of much concern. For magneto-chemical considerations, of course, such an approach would be inappropriate and the two contributions would have to be distinguished.
 - ¹⁹ P. W. Anderson, *Phys. Rev.* **86**, 694 (1952).
 - ²⁰ B. Bernu, C. Lhuillier, and L. Pierre, *Phys. Rev. Lett.* **69**, 2590 (1992).
 - ²¹ J. Schnack and M. Luban, *Phys. Rev. B* **63**, 014418 (2000).
 - ²² O. Waldmann, *Phys. Rev. B* **65**, 024424 (2002).
 - ²³ For the discussion of the effect of the magnetic anisotropy the ratio D/J is the relevant quantity. However, its effect also depends on the number N , and spin length s , of the spin centers, which has to be taken into account if one wants to compare the situation for different wheels. A better quantity is the so-called tunneling action $S_0/\hbar = Ns\sqrt{2D/J}$, as obtained in a semi-classical calculation.^{25,26} The semiclassical theory also gives the criterion $S_0/\hbar > 4$ for the crossover to the Néel-vector tunneling regime, which for CsFe₈ is $D/J > 0.02$.
 - ²⁴ B. Barbara and E. M. Chudnovsky, *Phys. Lett. A* **145**, 205 (1990).
 - ²⁵ A. Chiolero and D. Loss, *Phys. Rev. Lett.* **80**, 169 (1998).
 - ²⁶ F. Meier and D. Loss, *Phys. Rev. B* **64**, 224411 (2001).
 - ²⁷ R. W. Saalfrank, I. Bernt, E. Uller, and F. Hampel, *Angew. Chem. Int. Ed. Engl.* **36**, 2482 (1997).
 - ²⁸ P. Lecheminant, B. Bernu, C. Lhuillier, L. Pierre, and P. Sindzingre, *Phys. Rev. B* **56**, 2521 (1997).
 - ²⁹ O. Waldmann, *Europhys. Lett.* **60**, 302 (2002).
 - ³⁰ A. Furrer and H. U. Güdel, *Phys. Rev. Lett.* **39**, 657 (1977).
 - ³¹ O. Waldmann, *Phys. Rev. B* **68**, 174406 (2003).
 - ³² A. Furrer and H. U. Güdel, *J. Magn. Magn. Mater.* **14**, 256 (1979).
 - ³³ H. U. Güdel, in *Magneto-Structural Correlations in Exchange-Coupled Systems*, edited by R. D. Willet (Reidel, Amsterdam, 1985), p. 325.
 - ³⁴ O. Waldmann and H. U. Güdel, *Phys. Rev. B* **72**, 094422 (2005).
 - ³⁵ O. Waldmann, *Phys. Rev. B* **71**, 094412 (2005).
 - ³⁶ P. J. Brown, in *Neutron Data Booklet*, edited by A. J. Dianoux and G. Lander (Institute Laue-Langevin, Grenoble, 2001).
 - ³⁷ The assignment of the various transitions forming the spectrum of Fig. 8 is as follows [compare also with Fig. 4(b)]. Peaks I and II correspond to the two possible transitions between the $S = 0$ and $S = 1$ multiplets: $|0, 0\rangle \rightarrow |1, 0\rangle$ and $|0, 0\rangle \rightarrow |1, \pm 1\rangle$. The peaks III, IV and V arise from the five transitions between the $S = 1$ and $S = 2$ multiplets. In order of increasing energy, peak IV: $|1, \pm 1\rangle \rightarrow |2, 0\rangle$ and $|1, \pm 1\rangle \rightarrow |2, \pm 1\rangle$, peak V: $|1, \pm 1\rangle \rightarrow |2, \pm 2\rangle$, peak III: $|1, 0\rangle \rightarrow |2, 0\rangle$ and $|1, 0\rangle \rightarrow |2, \pm 1\rangle$. Finally, peak VI is produced by six of the eight possible transitions between the $S = 2$ and $S = 3$ multiplets: $|2, \pm 1\rangle \rightarrow |3, 0\rangle$, $|2, 0\rangle \rightarrow |3, 0\rangle$, $|2, \pm 1\rangle \rightarrow |3, \pm 1\rangle$, $|2, 0\rangle \rightarrow |3, \pm 1\rangle$, $|2, \pm 2\rangle \rightarrow |3, \pm 3\rangle$, and $|2, \pm 1\rangle \rightarrow |3, \pm 2\rangle$. Concerning the two remaining transitions, transition $|2, \pm 2\rangle \rightarrow |3, \pm 1\rangle$ (at 2.30 meV) coincides with the transition $|1, 0\rangle \rightarrow |2, \pm 1\rangle$ within the resolution of Fig. 8(a), and transition $|2, \pm 2\rangle \rightarrow |3, \pm 2\rangle$ appears as a weak satellite to peak III at 2.52 meV.
 - ³⁸ F. Cinti, M. Affronte, and A. G. M. Jansen, *Eur. Phys. J. B* **30**, 461 (2002).
 - ³⁹ S. Carretta, J. van Slageren, T. Guidi, E. Livioti, C. Mondelli, D. Rovai, A. Cornia, A. L. Dearden, F. Carsughi, M. Affronte, C. D. Frost, R. E. P. Winpenny, D. Gatteschi, G. Amoretti, and R. Caciuffo, *Phys. Rev. B* **67**, 094405 (2003).
 - ⁴⁰ O. Waldmann, R. Koch, S. Schromm, P. Müller, I. Bernt, and R. W. Saalfrank, *Phys. Rev. Lett.* **89**, 246401 (2002).
 - ⁴¹ O. Waldmann, C. Dobe, S. T. Ochsenein, H. U. Güdel, and I. Sheikin, *Phys. Rev. Lett.* **96**, 027206 (2006).
 - ⁴² G. Carver, O. Waldmann, C. Dobe, H. U. Güdel, and A. L. Barra (unpublished).
 - ⁴³ R. Bircher, G. Chaboussant, A. Sieber, H. U. Güdel, and H. Mutka, *Phys. Rev. B* **70**, 212413 (2004).
 - ⁴⁴ The parameters D_2 and B_4^0 relate to the effective Hamiltonian for the $S = 2$ multiplet $\hat{H}_{S=2} = D_2[\hat{S}_z^2 - 1/3S(S+1)] + B_4^0\hat{O}_4^0(S)$, where $\hat{O}_4^0(S)$ is a Stevens operator.⁴⁵
 - ⁴⁵ A. Abragam and B. Bleaney, *Electron Paramagnetic Resonance of Transition Ions* (Clarendon Press, Oxford, 1970).
 - ⁴⁶ W. Wernsdorfer, N. Aliaga-Alcalde, D. N. Hendrickson, and G. Christou, *Nature* **416**, 406 (2002).
 - ⁴⁷ S. Hill, R. S. Edwards, N. Aliaga-Alcalde, and G. Christou, *Science* **302**, 1015 (2003).
 - ⁴⁸ A. Sieber, D. Foguet-Albiol, O. Waldmann, S. T. Ochsenein, R. Bircher, G. Christou, F. Fernandez-Alonso, H. Mutka, and H. U. Güdel, *Inorg. Chem.* **44**, 6771 (2005).